Article

Journal of
Nanoscience and Nanotechnology
Vol. 15, 694–702, 2015
www.aspbs.com/jnn

Impact of Si^{4+} Ions Doping on the Electrochemical Cycling Performance of $NiTiO_3$ as Anodes for Li-Ion Batteries

V. D. Nithya[1], R. Kalai Selvan[1,*], K. Karthikeyan[2,3], and Y. S. Lee[2]

[1] *Solid State Ionics and Energy Devices Laboratory, Department of Physics, Bharathiar University, Coimbatore 641046, India*
[2] *Faculty of Applied Chemical Engineering, Chonnam National University, Gwang-Ju 500-757, Korea*
[3] *Department of Mechanical and Materials Engineering, The University of Western Ontario, London, Ontario, N6A 5B9, Canada*

Pristine and Si^{4+} doped $NiTiO_3$ are successfully synthesized by molten salt method and electrochemically characterized for its use as an anode material for Li-ion batteries. The X-ray diffraction (XRD) results enumerates that the lattice parameter and the cell volume decreases upon the addition of Si^{4+} due to its smaller ionic radius. The presence of Si^{4+} in $NiTiO_3$ structure was also confirmed using FTIR analysis, which showed the stretching vibrations of Si—O at ~ 1008 cm^{-1}. The SEM images reveal that the $NiTiO_3$ particles are in micrometer range and the size of the particle is found to be decrease after Si^{4+} addition. The electrical studies infers an enhancement in the conductivity from 4.4×10^{-7} $S \cdot cm^{-1}$ to 1.7×10^{-6} $S \cdot cm^{-1}$ on dopant addition. The initial discharge capacity of $NiTiO_3$ is found to be 1257 mA h g^{-1} and there is a capacity fading on consecutive cycles. $NiTi_{0.9}Si_{0.1}O_3$ enhances the cyclic performances and a constant capacity around 400 mA h g^{-1} is maintained, a very good reversibility with almost 100% efficiency is observed elucidating the fact that almost all the Li ions intercalated are successfully de-intercalated during the discharge process.

Keywords: Lithium Ion Batteries, Anode, Silicon, $NiTiO_3$.

1. INTRODUCTION

Lithium ion batteries (LIB) are most promising energy storage device due to its high energy density, low self discharge, long cycle life and hence found major role in many applications such as in mobile industry, computer applications, digital cameras, stationery and many other portable applications. However its usage is limited in the case of electric/hybrid vehicles applications due to the lack of sufficient power density which is determined by the faster charge discharge rates necessary to meet its demand. Recently, many researches are focused on finding an alternative electrode materials for LIB. The commercially available batteries utilizes graphite as negative electrode, which shows excellent cycling behaviour, long cycle life and low cost. The major drawback is being it possesses a low theoretical capacity of ~ 372 mA h g^{-1}which is not enough to meet today's need. So, there is an alternative search for the material that could exhibit higher capacity along with improved life. The alternatives are Si, Sn, and Ge based materials which are electrochemically alloyed with lithium and result in formation of reversible Li_xSi, Li_xSn, and Li_xGe where x denotes the number of moles of lithium participated for energy storage. These alloy anodes delivers high specific capacity of about 2–10 times higher than the graphitic anodes. The major drawback of these materials is that there is an enormous volume changes occurring on electrode during Li alloying/de-alloying that causes cracks on the electrode surface which decreases its cycle life.[2–4] Hence efforts are taken to overcome these drawbacks such as the usage of multiphase alloy anodes or mixing the active and inactive components in which the inactive component is responsible for regulating the volume changes or core shell nanocomposites such as Cu_6Sn_5–TiC–C nanocomposite alloy,[5] Cu_2-Sb@C[6] etc.

*Author to whom correspondence should be addressed.

 1533-4880/2015/15/694/009 doi:10.1166/jnn.2015.9165

with excellent cyclability. In this line, one dimensional metal oxides such as Co_3O_4,[7] NiO,[8] Fe_3O_4,[9] Mn_2O_3,[10] SnO_2,[11] TiO_2,[12] AMn_2O_4 (Co, Ni, Zn),[13] MnO[14] are considered as promising negative electrodes for LIB which provides high capacity along with better rate performances. The major advantage of these metal oxides in LIB application is that there will be a minimum disruption in the material on Li ion intercalation during the charge/discharge process. Some of these transition metal oxides like NiO, CuO, FeO, and CoO undergo conversion reaction since these metal oxides can't form alloy with lithium since due to the lack of sufficient voids for Li ion insertion/de-insertion. These transition metal oxides undergo conversion reaction, forming metal nano particles embedded in the Li_xO matrix upon discharge. The Li_xO matrix is completely decomposed and the metal nano particles are converted into their respective oxides on further charging, thereby minimizing the volume changes and hence excellent electrochemical stability can be achieved even after hundreds of cycles.

Research works on anode materials for LIB in the recent days are mainly focussed on titanium based anode materials such as $Li_4Ti_5O_{12}$, TiO_2, and $NaLi_2Ti_6O_{14}$, $Li_2Ti_6O_3$ etc for its usage in hybrid electric vehicles applications etc. The structural changes upon Li ion intercalation/de-intercalation are almost negligible in the case of $Li_4Ti_5O_{12}$ and less than 4% for TiO_2[15] which extend its cycle life offered by their outstanding structural stability.[16–19] These metal titanates are promising material due to their high safety, low cost, long cycle life, electrode potential values matches with the available cathode material, structurally stable etc. However, its low diffusion coefficient of Li ions and poor electrical conductivity limits them from being used in high power application. Several efforts has been focussed to improve these difficulties such as synthesizing materials in nanometer size or doping with alio-valent metal ions or fabricating polymer/metal oxide nano composites etc.

In this sequence of metal titanates, our present research work is focussed on synthesizing nickel titanate, $NiTiO_3$ using molten salt method which is believed to deliver high power, long cycle, extreme safety and optimum electrode potential. $NiTiO_3$ belongs to ABO_3 type ilmenite structure with both the ions Ni and Ti are of approximately equal sizes.[20] $NiTiO_3$ has its potential application in variety of fields such as in photo catalytic application, metal air batteries, gas sensors, electrodes for solid oxide fuel cells[21–23] etc. And this is the first report for ilmenite $NiTiO_3$ applied as an anode material for Li ion batteries.

$NiTiO_3$ was synthesized by various techniques such as sol–gel method,[24] pechini process,[25] co-precipitation method,[26] solution combustion technique,[27] polymeric precursor method[28] etc. In the present work, molten salt synthesis method was employed since it is liable to synthesis materials with desired morphologies which does not require any complicated set up. The major drawback associated with these metal oxides is that they possess poor electronic conductivity and which could be rectified by increasing the interlayer spacing efficient for easier Li ion insertion/de-insertion, by either synthesizing materials in the nano meter range or doping with alio valent metal ions or coating the materials with conductive materials such as carbon etc. In the present work, doping of Si^{4+} for Ti^{4+} site was employed to enhance the electronic conductivity thereby improving the electrochemical performance of the pristine material.

In this paper, we reported the synthesis of $NiTiO_3$ and 0.1 mole percentage of Si doped $NiTiO_3$ ($NiTi_{0.9}Si_{0.1}O_3$) by simple molten salt method and characterized using various techniques such as XRD, FTIR, and SEM. The electrical study was performed using a.c. impedance spectroscopic technique and the electrochemical performance of the prepared materials was carried out by charge–discharge studies cycled between 0.0–3.0 V. The preliminary study on the theoretical capacity of spinel lithium titanate at lower potential was done by Ge et al.[29] that gives an idea to achieve higher specific capacity when discharged to lower potentials. The theoretical capacity for the material discharged to 0 V would be higher than for discharged to 1 V due to the increase in the number of Li ion intercalated/de-intercalated upon discharged to 0 V.[30, 31]

2. EXPERIMENTAL DETAILS

$NiTiO_3$ was prepared by simple molten salt synthesis method. For the material preparation, stoichiometric amounts of the starting precursors NiO and TiO_2 were taken and ground well using mortar and pestle for about half an hour. In to the above mixture, the fused salts of NaCl and KCl in the molar ratio of 1:1 was added and again ground for another half an hour to get a well milled powder. The above mixture was placed in a quartz crucible and placed in the furnace and heated at 850 °C for 10 h to get the resultant product. The reaction takes place in the liquid medium due to the presence of molten salts. The advantage of this method is that the reaction rate gets enhanced which decreases the reaction temperature when compared to the conventional solid state reaction and possibility of obtaining particles with increased homogeneity. The resultant product was washed several times with double distilled water and ethanol to remove the residual chloride salts. It was then dried at 120 °C for 1 hour and utilised for further characterisations. The same procedure was adopted for the preparation of $NiTi_{0.9}Si_{0.1}O_3$, in which sodium metasilicate ($Na_2SiO_3 \cdot 9H_2O$) was used as silicon source.

2.1. Structural and Morphological Characterization

The X-ray Diffraction (XRD) studies were carried out using XPERT-PRO diffractometer system with Cu Kα

radiation ($\lambda = 1.5405$ Å) at 30 mA and 40 KV. The lattice parameter values were calculated using UNITCELL software. The Fourier Transform Infra-red (FT-IR) spectra were recorded using Avarter model FT-IR Spectrometer in the range of 4000–400 cm^{-1}. The Scanning Electron Microscopic (SEM) images were recorded using Hitachi-S3000H-SEM model. The a.c. impedance spectroscopy was performed by using HIOKI 3532 LCR HITESTER in the frequency range from 50 Hz–10 KHz. For this, the powder was pressed into pellets of diameter 1 cm and being sandwiched between two metal electrodes for measurements.

2.2. Electrochemical Measurement

For the electrochemical characterization of $NiTiO_3$ and $NiTi_{0.90}Si_{0.10}O_3$, the electrodes were prepared by mixing the active material with Super b black, PVDF in the weight ratio of 80:10:10 using *N*-methyl 2-pyrrolidone (NMP) as solvent to form slurry which was coated on pure aluminium foil and dried for 4 hr in vacuum oven. The dried electrode was used as the anode, the electrochemical cells were assembled in an argon filled atmosphere with Li metal as cathode, micro porous membrane (CELGRAD 3501) as separator in 1 M $LiPF_6$ in ethylene carbonate (EC): Diethylene carbonate (DEC) with 1:1 vol% as an electrolyte. The fabricated coin cells were charged to 3.0 V versus Li/Li^+ and then discharged to 0.00 V versus Li/Li^+ at a current density of 0.4 mA/cm^2 (Arbin cycler, USA).

3. RESULTS AND DISCUSSION

3.1. X-Ray Diffraction (XRD)

In order to examine the effect of Si addition on the structural characteristics of pristine $NiTiO_3$, XRD characterizations were carried out using Cu-Kα radiation ($\lambda = 1.5405$ Å). Figure 1(a) and (b) shows the X-ray diffraction pattern of $NiTiO_3$ and $NiTi_{0.90}Si_{0.10}O_3$. The sharp peaks show the highly crystalline nature of the materials. The peaks observed at $2\theta = 24.03$, 32.99, 35.548, 40.76, 49.34, 53.90, 57.35, 62.35, 63.97, 71.65, 75.7 corresponds to the lattice planes of (012), (104), (110), (113), (024), (116), (018), (124), (300), (10 10), (217) respectively.[32] The observed peaks are well matched with standard JCPDS file No. 83-0198 which corresponds to the rhombohedral crystal structure with $R\bar{3}$ space group. It is also observed that, there is a segregation of SiO_2 impurity phase which indicates that the dopant couldn't able to enter into the lattice site of pristine $NiTiO_3$.[33]

The magnified peak position of (1 0 4) plane is shown in Figure 2. It is to be noted that shift in the peak towards the lower angles was observed upon Si addition on $NiTiO_3$. As the angle (θ) becomes smaller, the atomic layer separation (d) gets increased which is favourable for easier insertion/de-insertion of Li ions into the lattice[34] as shown in Bragg's equation,

$$2d \sin\theta = n\lambda \quad (n = 1, 2, 3 \ldots) \tag{1}$$

where d is the inter-planar spacing, θ is the diffraction angle, λ is the X-ray wavelength. Therefore it is believed that the $NiTi_{0.90}Si_{0.10}O_3$ would possess better electrochemical performance than that of the parent $NiTiO_3$. The calculated lattice parameter values are $a = 5.0288$ Å, $c = 13.7827$ Å for $NiTiO_3$ and $a = 5.0258$ Å, $c = 13.7851$ Å for $NiTi_{0.90}Si_{0.10}O_3$, respectively. The cell volume calculated using these lattice parameter values is found to be 301.8614 $Å^3$ and 301.4838 $Å^3$ for $NiTiO_3$ and $NiTi_{0.90}Si_{0.10}O_3$ respectively. As expected, the lattice parameter values and the cell volume gets decreased on addition of dopant which is due to the fact that the ionic radii of Si^{4+} (0.42 Å) being smaller than that of the Ti^{4+} (0.68 Å).[35]

The lattice density values are calculated to be 5.1006 and 5.0407 g/cm^3 for $NiTiO_3$ and $NiTi_{0.90}Si_{0.10}O_3$ respectively. It is observed that, the lattice density value is smaller for $NiTi_{0.90}Si_{0.10}O_3$ compared with $NiTiO_3$ since

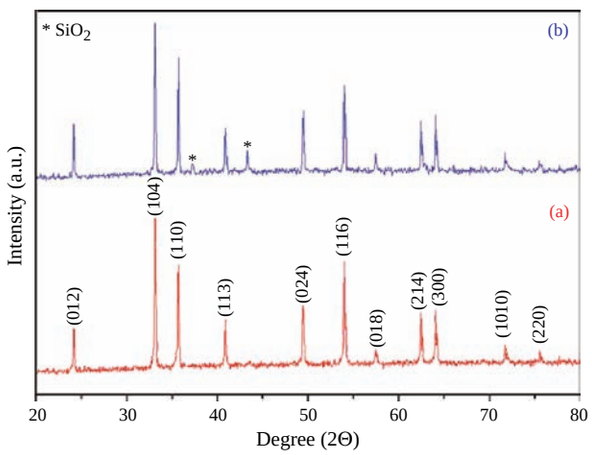

Figure 1. XRD pattern of (a) $NiTiO_3$ and (b) $NiTi_{0.90}Si_{0.10}O_3$.

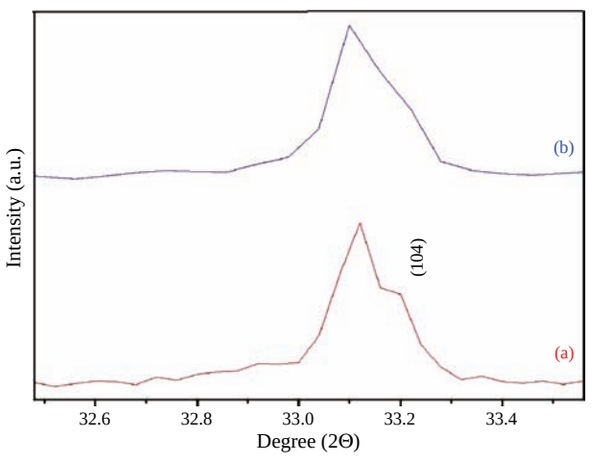

Figure 2. Magnified image of high intensity (1 0 4) plane spectra of (a) $NiTiO_3$ and (b) $NiTi_{0.90}Si_{0.10}O_3$.

the atomic weight of Si (28.085 g) being smaller than Ti (47.867 g). The crystallite size calculated by using Scherrer formula is in the range of nano meters, 66 nm and 45 nm for $NiTiO_3$ and $NiTi_{0.90}Si_{0.10}O_3$. It is found that the crystallite size is decreased on dopant addition. It is known that when the crystallite size decreases then automatically the surface area gets enhanced. The surface area could be calculated using the average crystallite size with the aid of the formula,

$$S = \frac{6}{\rho \times d}(\mathrm{m^2/g}) \tag{2}$$

where ρ is lattice density (in g/cm^3), d is the crystallite size (in microns). The calculated values of surface area for $NiTiO_3$ and $NiTi_{0.90}Si_{0.10}O_3$ are 19 and 26 m^2/g. It is seen that, the surface area gets increased for $NiTi_{0.90}Si_{0.10}O_3$ than the undoped $NiTiO_3$ sample. When the particle size gets decreased then the surface area could be enhanced, this facilitates the Li ion diffusion to be faster due to the decreased the diffusion path lengths. Hence it is expected that $NiTi_{0.90}Si_{0.10}O_3$ would show better electrochemical performance than pristine $NiTiO_3$.

Normally the tolerance factor is calculated in order to study the stability of the ABO_3 type compounds. The tolerance factor (t) for ABO_3 type ilmenite can be given as

$$t = \frac{1}{3}\left(\frac{(\sqrt{2}+1)R_o + R_B}{R_o + R_A} + \frac{\sqrt{2}R_o}{R_o + R_B}\right) \tag{3}$$

where R_A, R_B, R_o are the radius of ion A, B and O^{2-} (in nano meters). Here $R_A(R_{Ni}^{2+}) = 0.069$ nm, $R_B(R_{Ti}^{4+}) = 0.06$ nm, $R_O(R_O^{2-}) = 0.1472$ nm.

The tolerance factor value (t) for the structurally stable ABO_3 ilmenite type compound should be higher than 0.80. The obtained t value for $NiTiO_3$ and $NiTi_{0.90}Si_{0.10}O_3$ are 0.9608 and 1.0043 respectively. It is to be noted that the tolerance factor value increases upon doping which infers that the doping has improved the stability of the prepared $NiTiO_3$ to greater extent.[36]

The electrical conductivity of the materials is mainly determined by the defect concentrations present in the material. The defect concentration present in the material is directly related to the micro strain that could be calculated using the relation given by,

$$\text{Microstrain, } \varepsilon\% = \frac{\beta}{4\tan\theta} \tag{4}$$

where β is the full width half maximum for the corresponding high intensity (1 0 4) plane. The value of micro strain calculated for $NiTiO_3$ and $NiTi_{0.90}Si_{0.10}O_3$ are 0.13% and 0.15%. It is reported in the case of polycrystalline material,[37] there is an increase in micro strain value with decrease in the grain size. As the grain size decreases, the defect concentration gets high. A similar kind of result is observed in our case too. It is observed that the grain size decreases on the addition of dopant Si. Hence, it could be concluded that the defect concentration that is associated with the micro strain is increased upon dopant addition.

3.2. FT-IR Analysis

The functional groups present in the material and the effect in the absorption bands upon the addition of dopants are analysed from FTIR analysis. The FTIR signature of $NiTiO_3$ and $NiTi_{0.90}Si_{0.10}O_3$ scanned in the wave number region between 400–4000 cm^{-1} are given in Figures 3(a) and (b). $NiTiO_3$ exhibited an absorption band at $\sim$438 cm^{-1} corresponds to the Ti—O bond stretching in TiO_6 octahedral (shown in Fig. 3(a)).[32] The absorption bands shift to the larger wave numbers 463 cm^{-1} on the addition of dopant in the case of $NiTi_{0.90}Si_{0.10}O_3$ as shown in Figure 3(b). This is due to the fact that, on dopant addition, there is a decrease in the cell volume as evident from XRD analysis, which causes Ti—O bond to become stronger. Since, the binding energy of Ti—O bond gets increased and hence the wave numbers shift to larger values. It is evident that the dopant affects the vibration of crystal lattice which is the indication of the peak shifting in the spectrum. The presence of an additional absorption bands at $\sim$1008 cm^{-1} for $NiTi_{0.90}Si_{0.10}O_3$ is due to the asymmetric stretching vibrations of the Si—O band,[38] revealing the presence of silicon phase in the crystal lattice of $NiTiO_3$ material. The absorption band at 2923 cm^{-1} in both the spectra is due to the symmetric and asymmetric stretching modes of C—H bonds.[39] The additional bands at 3400 and 3775 cm^{-1} attributes to the O—H stretching vibration of adsorbed water.[40]

3.3. Morphological Analysis

The SEM images and the corresponding particle size histogram of parent $NiTiO_3$ and $NiTi_{0.90}Si_{0.10}O_3$ are presented in Figure 4. Figures 4(a) and (b) presents the SEM image and particle size histogram of parent $NiTiO_3$ material. As evidenced from Figure 4(a), the particles of pure $NiTiO_3$ are spherical in shape and homogeneous without any agglomeration. Since the molten salt synthesis involved solution based synthesis at high temperature, it resulted in the formation of particles with uniform morphology,

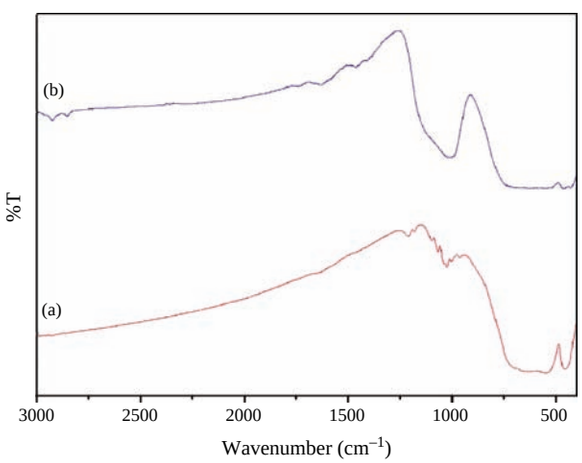

Figure 3. FTIR spectra of (a) $NiTiO_3$ and (b) $NiTi_{0.90}Si_{0.10}O_3$.

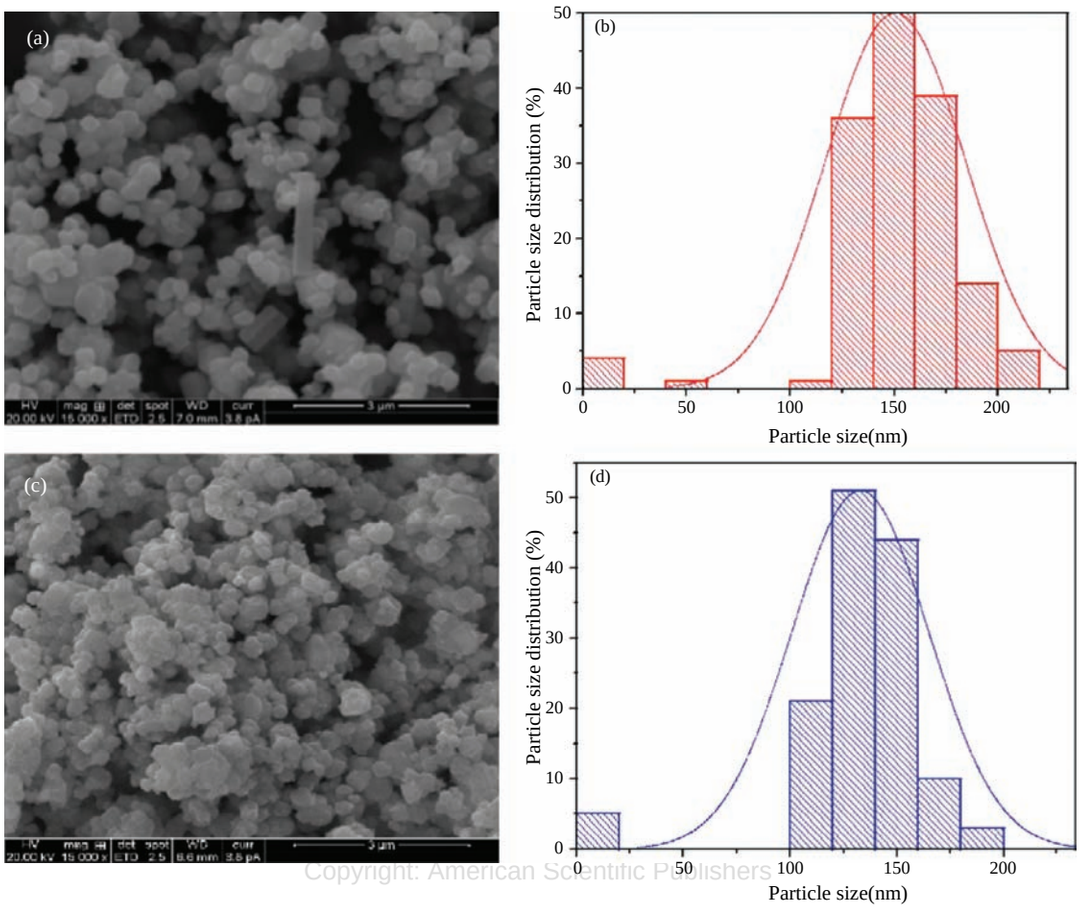

Figure 4. SEM image and corresponding particle size histogram of (a) and (b) $NiTiO_3$ and (c) and (d) $NiTi_{0.90}Si_{0.10}O_3$.

preventing the particle agglomeration. Moreover, the particles will be in the micrometer range at those high heating atmospheres. The image shows the well crystalline nature of the material. The particles are found to be in micrometer range. The particle size histogram shows that the maximum number of particles are found to be in the range of 140–160 nm. Figures 4(c) and (d) shows the SEM image and corresponding particle size histogram of $NiTi_{0.90}Si_{0.10}O_3$ material. Shown in Figure 4(c), the addition of dopants on $NiTiO_3$ causes the reduction in particles size as well as prevents agglomeration. It is evident from the particle size histogram that the particle sizes are reduced upon addition of dopants, the maximum number of particles are found in the range of 120–140 nm. The addition of even lower amount of dopant has reduced to the particle size to a certain limit. It is well known that the material with high crystalline nature is favourable for prolonged cycling performances.

3.4. Electrical Conductivity Analysis

The electrical behaviour of the material at room temperature over a wide range of frequencies is studied using a.c. impedance spectroscopic analysis. In general, the Nyquist plot appears as a succession of semi-circle representing the electrical conduction mechanism that occurs due to either the grain or grain boundary or interfacial polarisation. Figure 5 shows the Nyquist plot of $NiTiO_3$ and $NiTi_{0.90}Si_{0.10}O_3$ materials measured at room temperature. A semi-circle in high frequency region followed by a tail in low frequency region is observed in the Nyquist plot for both the materials. The semi-circle in high frequency region implies the resistance of the material is due to grain conduction. This semi-circle behaviour is due to the contribution of parallel combination of both bulk capacitance C_b and bulk resistance R_b. There is no semi circle found in the low frequency region implying that no grain boundary conduction in the material and is purely due to the bulk conduction. The tail appears in the high frequency region is due to the electrode-electrolyte interfacial polarisation at the blocking electrodes. The bulk resistance R_b of the material is calculated by intercepting the semi-circular arc with real axis and the values are measured to be $4.54 \times 10^5\ \Omega$ and $1.14 \times 10^5\ \Omega$ respectively. The value of bulk capacitance is calculated using the relation $2\pi\gamma_{max}R_bC_b = 1$ and it is in the order of pico Farads. The bulk capacitance values for $NiTiO_3$ and $NiTi_{0.90}Si_{0.10}O_3$

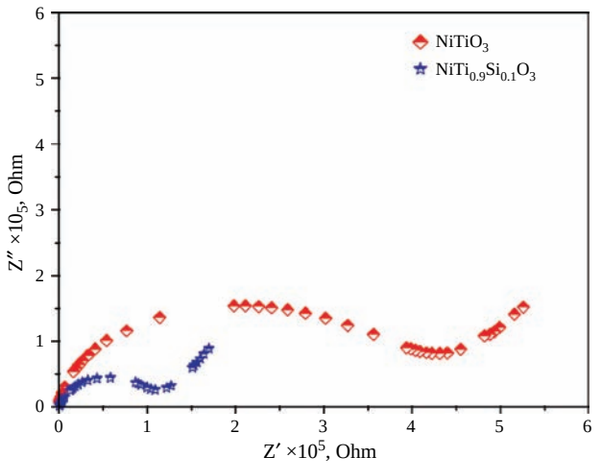

Figure 5. Nyquist plot of $NiTiO_3$ and $NiTi_{0.90}Si_{0.10}O_3$ at room temperature.

are found to be 32 pF and 41 pF respectively. This higher capacitance value reveals that the conduction is through bulk of the material. The value of conductivity $\sigma_{d.c}$ ($S \cdot cm^{-1}$) could be calculated using the measured R_b values using the relation given by,

$$\sigma_{dc} = \frac{L}{R_b A} \tag{5}$$

where L is the thickness and A is the area of cross section of the pelletized sample (in cms). The calculated values are 4.38×10^{-7} $S \cdot cm^{-1}$ and 1.74×10^{-6} $S \cdot cm^{-1}$ for $NiTiO_3$ and $NiTi_{0.90}Si_{0.10}O_3$, respectively. The value of d.c. conducivity is found to be higher for $NiTi_{1.9}Si_{0.1}O_3$ than parent $NiTiO_3$ material. The reason beyond this is the addition of smaller size cation into the lattice site leads to the decreased lattice parameter values as evident from XRD analysis which causes easier hopping of charge carriers.[41]

The conductance spectra of $NiTiO_3$ and $NiTi_{0.90}Si_{0.10}O_3$ measured at room temperature are given in Figure 6. It is observed from the conductance spectra that there are two distinctive regions observed (i) low frequency d.c. conductivity region where the value of conductivity is found to be invariant with respect to the frequency and (ii) high frequency a.c. dispersion region. According to the jump relaxation model,[42] there is a short range pair wise hopping between the adjacent sites at the low frequency. And there is probability of forward and backward hopping together with the relaxation of ions at the high frequency dispersion region. The conductance spectra is found to obey the Jonscher's power law given by the equation,

$$\sigma(\omega) = \sigma_{d.c.} + A\omega^n \tag{6}$$

where $\sigma_{d.c.}$ is the d.c. conductivity, A the dispersion parameter, n the frequency exponent. The conductance spectra is non-linearly fitted to obtain the values of d.c. conductivity, A and n values. The value of d.c. conductivity observed

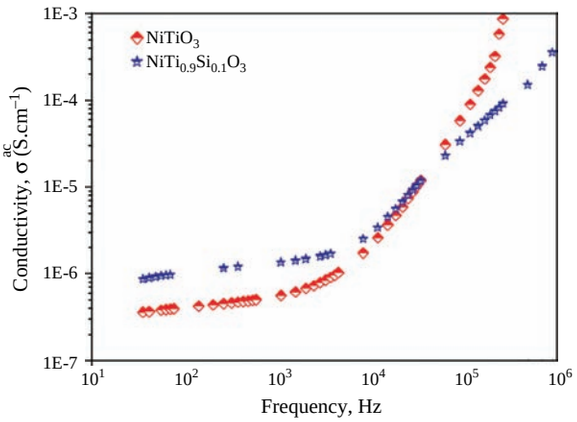

Figure 6. Conductance spectra of $NiTiO_3$ and $NiTi_{0.90}Si_{0.10}O_3$ at room temperature.

for $NiTiO_3$ and $NiTi_{0.90}Si_{0.10}O_3$ are 4.30×10^{-7} and 1.7×10^{-6} $S \cdot cm^{-1}$ respectively. The observed values are in consistence with the impedance spectral values. The value of n has a physical meaning that, if $n \leq 1$, then the hopping motion involves a translation motion with a sudden hopping whereas if $n \geq 1$, the hopping motion involves localised hopping.[43] The fitted conductance plot yields the value of n to be 1.4567 for $NiTiO_3$ which elucidate the fact that the hopping motion are translation in the parent material. The hopping motion involved in the case of $NiTi_{0.90}Si_{0.10}O_3$ is localised which is evident from the value of n i.e., 0.9666.

Using the fitted values, the hopping frequency (ω_p), carrier concentration (N) and carrier mobility (μ) are calculated using the relation given by,

$$\text{Hopping frequency, } \omega_p = \left(\frac{\sigma_{d.c.}}{A}\right)^{1/n} \tag{7}$$

$$\text{Carrier concentration, } N = \left(\frac{\sigma_{d.c} T}{\omega_p}\right) \tag{8}$$

$$\text{Carrier mobility, } \mu = \frac{\sigma_{d.c}}{Ne} \tag{9}$$

The value of hopping frequency obtained for $NiTiO_3$ and $NiTi_{0.90}Si_{0.10}O_3$ are 6.9578×10^3 Hz and 1.6673×10^4 Hz and the carrier mobility are 15.9306×10^{19} ($cm^2/V \cdot s$) and 38.302×10^{19} ($cm^2/V \cdot s$). It is to be observed that the hopping frequency gets enhanced in the case of $NiTi_{0.90}Si_{0.10}O_3$ which in turn enhances the carrier mobility. The increase in the hopping frequency and mobility causes the conductivity to be enhanced in $NiTi_{0.90}Si_{0.10}O_3$. The d.c. conductivity ($\sigma_{d.c}$) related to the hopping frequency is given by Barton-Nakajima-Namikawa (BNN) relationship,[44]

$$\sigma_{d.c} = NT^{-1}\omega_p \tag{10}$$

where N is the carrier concentration, ω_p is the hopping frequency which is nothing but the cross over frequency

from the d.c. conductivity region to the a.c. dispersion region. For a particular temperature, the d.c. conductivity ($\sigma_{d.c}$) is directly proportional to the hopping frequency of the charge carriers since the carrier concentration remains almost constant at that particular temperature. The conductivity values measured at identical condition shows enhanced value for $NiTi_{0.90}Si_{0.10}O_3$ compared with $NiTiO_3$, which is due to the increase in the density of mobile defects on the addition of dopant. As stated from the XRD results, the mobile defect density gets increased on the dopant addition due to decrease in the crystallite size.

The value of carrier concentration calculated using the above relation was 1.687×10^{-8} Scm^{-1} KHz^{-1} and 2.774×10^{-8} Scm^{-1} KHz^{-1} for $NiTiO_3$ and $NiTi_{0.90}Si_{0.10}O_3$ respectively. There is no much difference in the concentration; they are almost constant at room temperature since due to the isovalent ion substitution.

3.5. Electrochemical Charge–Discharge Analysis

Figures 7(a) and (b) shows the charge/discharge curves of $NiTiO_3$ and $NiTi_{0.90}Si_{0.10}O_3$ at a current density of 0.4 mA/cm^2 cycled between 3.0 to 0.00 V. Figure 7(a) shows the first six charge discharge cycles of $NiTiO_3$ in the voltage range given above. The first discharge profile shows a plateau with onset of potential at 1.1 V and the plateau sets at 0.88 V. The second plateau is observed with the potential onset at 0.55 and ends at 0.38 V. As seen, the initial discharge capacity of parent $NiTiO_3$ is found to be 1257 mA h g^{-1} that infers one formula unit of $NiTiO_3$ can host up to 7 moles of Li^+. The two phase reduction reactions that occurs is given by the equations,

$$NiTiO_3 + xLi^+ + xe^- \rightarrow NiO + Li_xTiO_2 \quad (11)$$

$$NiO + xLi^+ + xe^- \leftrightarrow Ni + Li_xO \quad (12)$$

During the second discharge, the capacity was decreased to 544 mAh/g. The voltage plateau observed in this case is 0.49 V that corresponds to the conversion reaction given by the Eq. (12). The discharge plateau at 0.49 V corresponds to the initial reduction of NiO to Ni and the formation of amorphous Li_2O.[45] During the conversion reaction, there is a formation/decomposition of electrochemically inert Li_2O along with the reduction/oxidation of metallic Ni particles. There is a destruction of the crystal structure occurs during the initial discharge and it is followed by the formation of metal nanoparticles embedded into the Li_2O. Although these Li_2O are electrochemically inert, they participate in the electrochemical reaction due to the embedded metallic Ni particles.[46] The capacity of the material in the second cycle during discharge is 544 mA h g^{-1} and during charging process is 514 mA h g^{-1}. The columbic efficiency corresponding to second cycle is 105%. The columbic efficiency is calculated using the relation given by,

$$\text{Coulombic efficiency, } \eta = \frac{\text{Specific Discharge capacity}}{\text{Specific charging capacity}} \times 100\% \quad (13)$$

The initial discharge capacity is 1257 mA h g^{-1} and the capacity decreases to 544 mA h g^{-1} during the second cycle. The observed capacity is only 46% of the initial discharge capacity. A high value of discharge capacity observed during first cycle is due to either the contribution of 10 wt% Super B black present in the electrode or traces of water present in the fresh electrode. The breakdown process occurs in the electrolyte solution like reduction of water present in the fresh electrodes after the initial cycle may be the reason for capacity fading from first cycle to second cycle.[47] The discharge capacities at the 5th cycle, 20th cycle, 25th cycles are 459 mA h g^{-1}, 175 mA h g^{-1}, 182 mA h g^{-1} respectively. A continuous fade in the capacity is observed for every consecutive cycles of the pristine $NiTiO_3$ material. The possible way that might reduce the capacity loss is structuring into suitable morphologies that could better accommodate the volume changes. In general, enhancement in the specific capacity, faster charge–discharge rate, and high Li ion diffusivity could be achieved in particles that possess nano

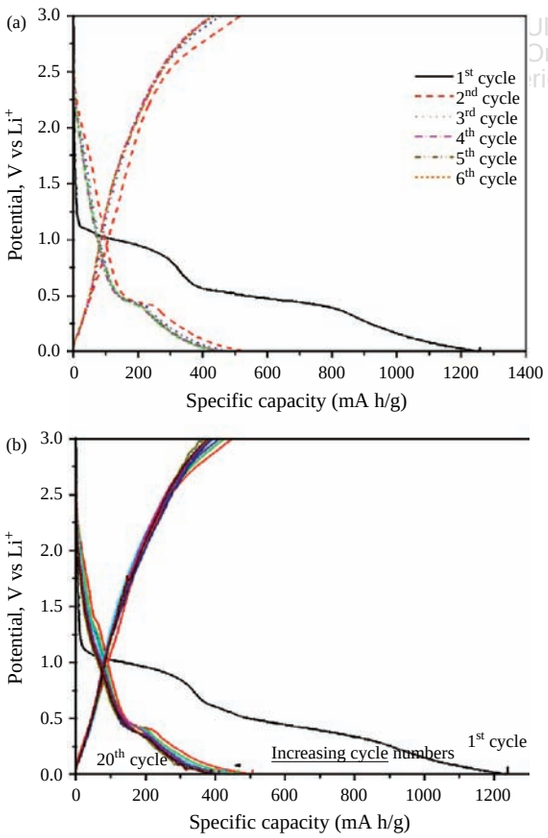

Figure 7. Charge–discharge curves of (a) $NiTiO_3$ and (b) $NiTi_{0.90}Si_{0.10}O_3$ at a current density of 0.4 mA/cm^2.

meter size with desirable morphologies. Another fact that could minimize the capacity loss is by altering the composition upon addition of multivalent ions in the material. In our work, substitution of electro active dopant ions into the material i.e., addition of 0.1 mole percentage of Si was adopted to improve the energy storing capability of parent $NiTiO_3$ material.

Figure 7(b) shows the first 20 charge discharge cycles of $NiTi_{0.90}Si_{0.10}O_3$. There are two distinct plateaus noticed in the initial discharge cycles as observed in the case of parent $NiTiO_3$. The electrochemical reaction that occurs in $NiTi_{0.90}Si_{0.10}O_3$ is similar to that of $NiTiO_3$. The initial discharge capacity is 1238 mA h g^{-1}. The discharge capacities of 5th, 10th, 15th and 20th cycles are 426 mA h g^{-1}, 418 mA h g^{-1}, 407 mA h g^{-1} and 385 mA h g^{-1} respectively. The corresponding cycling stability curve of $NiTiO_3$ and $NiTi_{0.90}Si_{0.10}O_3$ is given in Figures 8(a) and (b). Figure 8(a) shows the cycling stability curve of $NiTiO_3$ for 25 cycles. It is observed that there is a serious capacity fading observed upto 25 cycles. The cycling stability curve for $NiTi_{0.9}Si_{0.1}O_3$ is presented in Figure 8(b). It is to be also observed that, the $NiTi_{0.9}Si_{0.1}O_3$ material shows minimum fade in the discharge capacity values after 5 cycles. The specific capacity of around 400 mA h g^{-1} was maintained after 5 cycles. The minimization of the capacity loss occurred might be due to the presence of SiO_2 phase that effectively enhances the cycling behaviour of $NiTiO_3$. It is reported that the enhanced cycling performance of the material was due to the presence of SiO_2 phase in $Li_4Ti_5O_{12}$.[48] A similar kind of observation is noticed in case of $Li_4Ti_5O_{12}$, where a minimum amount of SiO_2 impurity is observed from the XRD pattern.[48] The formed SiO_2 impurity is coated as a thin film over the uniform shaped $Li_4Ti_5O_{12}$. Furthermore, since the change in particle size upon the addition of dopant is not too high, the size effect doesn't play major role on stabilizing the cyclic performance.[48] On the other hand, SiO_2 phase played a major role in maintaining the capacity. The columbic efficiency graph for $NiTi_{0.9}Si_{0.1}O_3$ is shown in Figure 8(c). The $NiTi_{0.9}Si_{0.1}O_3$ possesses high reversible capacity on cycling. The columbic efficiency was found to be almost 100% i.e., good reversibility for all the 20 cycles of $NiTi_{0.9}Si_{0.1}O_3$ which elucidates the fact that almost all the Li ions intercalated are successfully de-intercalated during the discharge process.

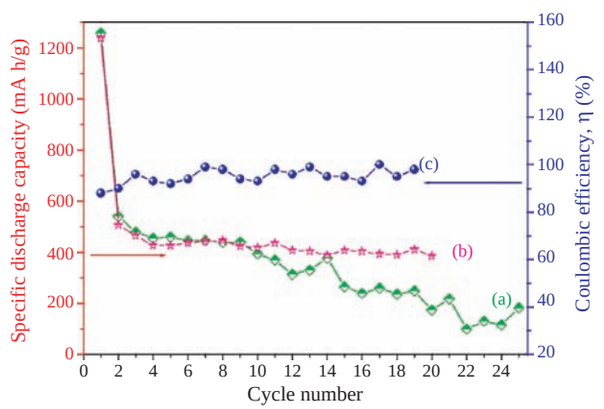

Figure 8. Cyclic stability of (a) $NiTiO_3$, (b) $NiTi_{0.90}Si_{0.10}O_3$ (c) Columbic efficiency of $NiTi_{0.9}Si_{0.1}O_3$.

The present work dealt with the substitution of electro active dopant ions into the material. Although the capacity loss has been minimized to a certain extent, still it is insufficient. Therefore, further studies are focussed on reducing the particle size to nano meter range and structuring into a well defined morphology that could minimize the capacity loss in order to enhance the both power density and energy density of the material.

4. CONCLUSION

$NiTiO_3$ and $NiTi_{0.90}Si_{0.10}O_3$ were successfully synthesized using molten salt method and utilized as anode materials for lithium ion batteries application. The XRD pattern of $NiTi_{0.90}Si_{0.10}O_3$ inferred the material was highly crystalline and possessed rhombohedra crystal structure along with the presence of SiO_2 peaks. There was a reduction in the particle size observed from the SEM image upon the addition of dopant. The materials possessed room temperature conductivity and it is 4.3×10^{-7} $S \cdot cm^{-1}$ and 1.7×10^{-6} $S \cdot cm^{-1}$ for $NiTiO_3$ and $NiTi_{0.90}Si_{0.10}O_3$ respectively. The electrochemical studies showed that the parent $NiTiO_3$ suffered from serious capacity loss. The formed SiO_2 in $NiTi_{0.90}Si_{0.10}O_3$ phase plays a main role on enhancing the cycling stability of the $NiTi_{0.90}Si_{0.10}O_3$ material. The columbic efficiency of $NiTi_{0.90}Si_{0.10}O_3$ was also found to be almost 100%. The above results predict that $NiTi_{0.90}Si_{0.10}O_3$ could be used as a suitable anode material for Li-ion batteries.

Acknowledgments: One of the authors (V. D. Nithya) deeply thanks the Department of Science and Technology (DST), New Delhi, India for providing fellowship under DST-INSPIRE program. One of the authors (RKS) would like to thank UGC for the financial support under Major Research Project (F. No: 41-838-2012 (SR)).

References and Notes

1. C. Wang, A. J. Appleby, and F. E. Little, *Journal of Electroanal. Chem.* 519, 9 (**2002**).
2. N. Ding, J. Xu, Y. Yao, G. Wegner, I. Lieberwirth, and C. Chen, *J. Power Sources* 192, 644 (**2009**).
3. M. Winter and J. O. Besenhard, *Electrochim. Acta* 45, 31 (**1999**).
4. C. K. Chan, X. F. Zhang, and Y. Cui, *Nano Lett.* 8, 307 (**2008**).
5. D. Applestone and A. Manthiram, *RSC Advances* 2, 5411 (**2012**).
6. Y. He, L. Huang, X. Li, Y. Xiao, G.-L. Xu, J.-T. Li, and S.-G. Sun, *J. Mater. Chem.* 21, 18517 (**2011**).
7. X. Wang, H. Guan, S. Chen, H. Li, T. Zhai, D. Tang, Y. Bando, and D. Golberg, *Chem. Commun.* 47, 12280 (**2011**).
8. H. Liu, G. Wang, J. Liu, S. Qiao, and H. Ahn, *J. Mater. Chem.* 21, 3046 (**2011**).

9. J. Liu, Y. Zhou, F. Liu, C. Liu, J. Wang, Y. Pan, and D. Xue, *RSC Advances* 2, 2262 **(2012)**.
10. Y. Deng, Z. Li, Z. Shi, H. Xu, F. Peng, and G. Chen, *RSC Advances* 2, 4645 **(2012)**.
11. J. S. Chen, L. A. Archer, and X. Wen (David) Lou, *J. Mater. Chem.* 21, 9912 **(2011)**.
12. Y. Chen, Q. Z. Huang, J. Wang, Q. Wang, and J. M. Xue, *J. Mater. Chem.* 21, 17448 **(2011)**.
13. F. M. Courtel, H. Duncan, Y. Abu-Lebdeh, and I. J. Davidson, *J. Mater. Chem.* 21, 10206 **(2011)**.
14. X. Li, D. Li, L. Qiao, X. Wang, X. Sun, P. Wang, and D. He, *J. Mater. Chem*. 22, 9189 **(2012)**.
15. M. Wagemaker, *J Am. Chem. Soc.* 125, 840 **(2003)**.
16. W. Dongmei, *Ionics* 18, 559 **(2012)**.
17. D. C. Johnson and A. L. Prieto, *J. Power Sources* 196, 7736 **(2011)**.
18. J. C. Perez-Flores, A. Kuhn, and F. Garcia-Alvarado, *J. Power Sources* 196, 1378 **(2011)**.
19. H.-W. Shim, D. K. Lee, I.-S. Cho, K. S. Hong, and D.-W. Kim, *Nanotechnology* 21, 255706 **(2010)**.
20. Y. M. Chiang, D. Birnie, and W. D. Kingery, Physical Ceramics, John Wiley & Sons Inc, New York **(1996)**, Vol. 34.
21. Y. Qu, W. Zhou, Z. Ren, S. Du, X. Meng, G. Tian, K. Pan, G. Wang, and H. Fu, *J. Mater. Chem.* 22, 16471 **(2012)**.
22. R. Fisch, *Phys Rev. B* 51, 11507 **(1995)**.
23. O. Yamamoto, Y. Takeda, R. Kanno, and M. Noda, *Solid State Ionics* 22, 241 **(1987)**.
24. D. J. Taylor, P. F. Fleigh, and R. A. Page, *Thin Solid Films* 408, 104 **(2002)**.
25. Y.-J. Lin, Y.-H. Chang, W.-D. Yang, and B.-S. Tsai, *J. Non-Cryst. Solids* 352, 789 **(2006)**.
26. A. Vadivel Murugan, Violet Samuel, S. C. Navale, and V. Ravi, *Mater. Lett.* 60, 1791 **(2006)**.
27. Y. Ni, X. Wang, and J. Hong, *Mater. Res. Bull.* 44, 1797 **(2009)**.
28. K. P. Loopes, L. S. Cavalcante, A. Z. Simoes, J. A. Varela, E. Longo, and E. R. Leite, *J. Alloys Compd.* 468, 327 **(2009)**.
29. H. Ge, N. Li, D. Li, C. Dai, and D. Wang, *J. Phys. Chem. C* 113, 6324 **(2009)**.
30. T.-F. Yi, Y. Xie, L.-J. Jiang, J. Shu, C.-B. Yue, A.-N. Zhou, and M.-F. Ye, *RSC Advances* 2, 3541 **(2012)**.
31. Y.-R. Jhan and J.-G. Duh, *Electrochim. Acta* 63, 9 **(2012)**.
32. M. S. Sadjadi, K. Zare, S. Khanamadzadeh, and M. Enhessari, *Mater Lett.* 62, 3679 **(2008)**.
33. X. Li, M. Qu, and Z. Yu, *J. Alloys Compds* 487, L12 **(2009)**.
34. G. Q. Liu, L. Wen, G. Y. Liu, Q. Y. Wu, H. Z. Luo, B. Y. Ma, and Y. W. Tian, *J. Alloys Compd* 509, 6427 **(2011)**.
35. R. D. Shannon, *Acta Cryst.* A32, 751 **(1976)**.
36. X. C. Liu, R. Hong, and C. Tian, *J. Mater Sci: Mater Electron* 20, 323 **(2009)**.
37. L. N. Patro and K.Hariharan, *Mater. Res. Bull.* 46, 732 **(2011)**.
38. M. A. Karakassides, D. Gournis, and D. Petridis, *Clay Minerals* 34, 429 **(1999)**.
39. M. N. Kamalasanan, N. Deepak Kumar, and S. Chandra, *J. Appl. Phys.* 76, 4603 **(1994)**.
40. N. Pavlovie, D. Kancho, K. M. Szecseny, and V. V. Srdic, *Process Appl. Ceram* 3, 88 **(2009)**.
41. C. T. G Petit, R. Lan, P. I. Cowin, and S. Tao, *J. Solid State Chem.* 183, 1231 **(2010)**.
42. P. S. Anantha and K. Hariharan, *Mater. Sci. Engg. B* 121, 12 **(2005)**.
43. B. Behera, P. Nayak, and R. N. P. Choudhary, *J. Alloys Compd.* 436, 226 **(2007)**.
44. B. K. Money and K. Hariharan, *Integr Ferroelectrics* 120, 75 **(2010)**.
45. X. Wang, X. Li, X. Sun, F. Li, Q. Liu, Q. Wang, and D. He, *J. Mater. Chem.* 21, 3571 **(2011)**.
46. P. P. Laruelle, S. S. Grugeon, L. Dupont, and J. M. Tarascon, *Nature* 407, 496 **(2000)**.
47. M. Kalbac, M. Zukalova, and L. Kavan, *J. Solid State Electrochem.* 8, 2 **(2003)**.
48. S. Jiang, B. Zhao, Y. Chen, R. Cai, and Z. Shao, *J. Power Sources* **(2013)**, 10.1016/j. jpowsour.2013.03.017.

Received: 12 April 2013. Accepted: 27 August 2013.